Volume 61
Number 87
11 November 2025
Pages 16877–17048

ChemComm

Chemical Communications

rsc.li/chemcomm

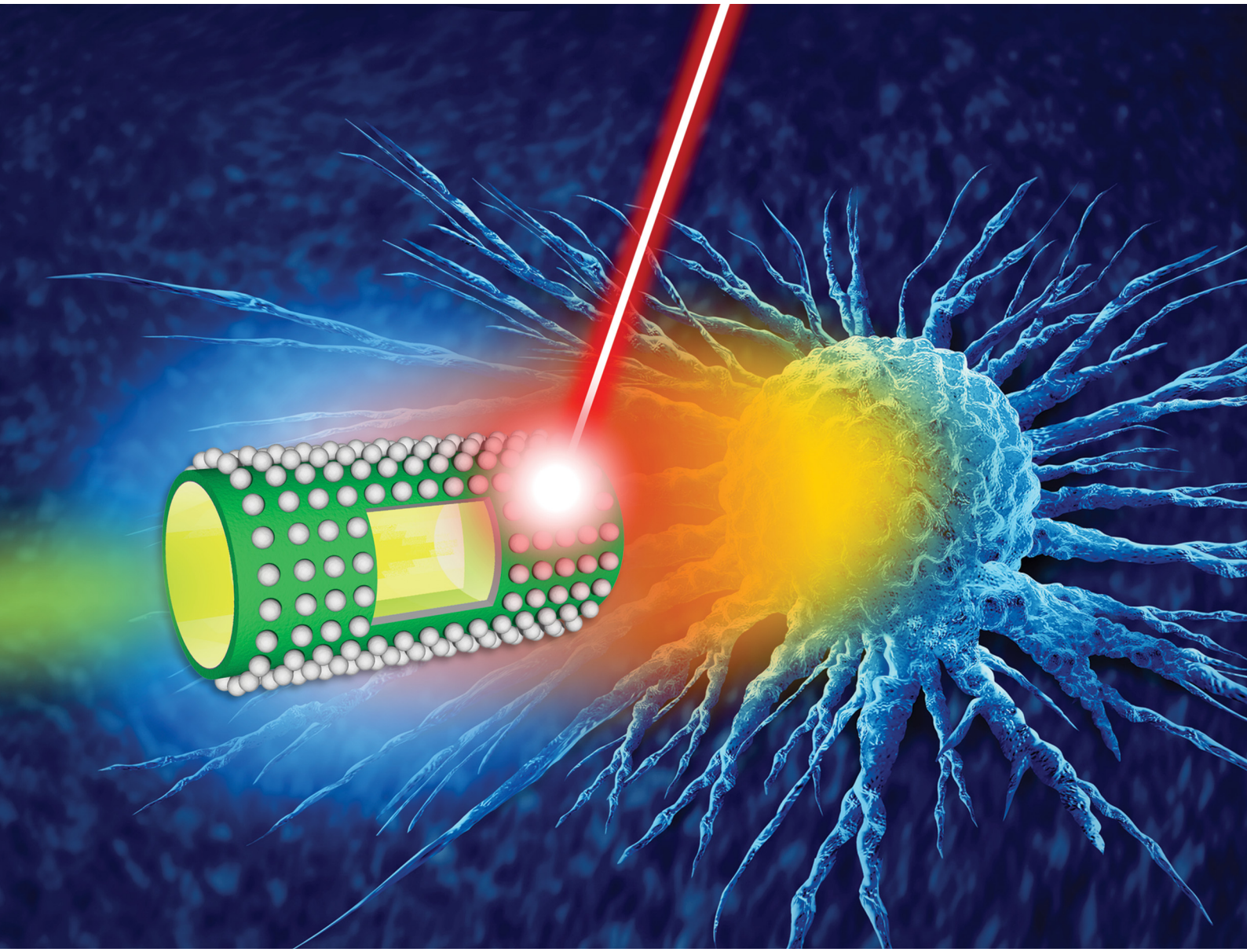

ISSN 1359-7345

ROYAL SOCIETY OF CHEMISTRY

FEATURE ARTICLE

Saki Batori and Teruyuki Komatsu

Photocurable polymer-based tubular micromotors: advancing toward life science applications

ChemComm

FEATURE ARTICLE

View Article Online
View Journal | View Issue

Cite this: *Chem. Commun.*, 2025, **61**, 16905

Photocurable polymer-based tubular micromotors: advancing toward life science applications

Saki Batori and Teruyuki Komatsu *

Micromotors—micrometer-scale objects capable of autonomous motion in aqueous environments—have emerged as promising tools in microtechnology and microrobotics. Among their structural variants, hollow tubular architectures are particularly attractive due to their multifunctional surfaces. A key challenge lies in advancing their practical application in life sciences. This review highlights recent progress in photocurable polymer-based tubular micromotors. Acrylic-resin tubes incorporating platinum nanoparticles (Pt tubes) were fabricated through a template-assisted process combining photopolymerization with wet layer-by-layer assembly. Protein-functionalized Pt tubes are propelled in H_2O_2 solutions *via* O_2 bubble generation, while catalase-modified tubes exhibit light-tunable propulsion. Remarkably, Pt tubes also self-propel in aqueous ammonia borane (NH_3BH_3) through H_2 bubble release, enabling lectin-coated micromotors to capture live cells without damage. Moreover, urease-driven tubes wrapped with doxorubicin-loaded liposomes demonstrate efficient anticancer activity under near-infrared irradiation. These findings underscore the potential of photocurable polymer-based tubular micromotors as versatile platforms for future biological and biomedical applications.

Received 10th September 2025,
Accepted 29th September 2025

DOI: 10.1039/d5cc05216e

rsc.li/chemcomm

1. Introduction

Research on nano- and micromotors capable of autonomous propulsion in aqueous media has advanced significantly over the past 15 years, resulting in diverse designs and synthetic strategies.[1–3] Micromotor morphologies include particles, wires, rods, sheets, and tubes. Among these, hollow cylinders

Department of Applied Chemistry, Faculty of Science and Engineering, Chuo University, 1-13-27 Kasuga, Bunkyo-ku, Tokyo, 112-8551, Japan.
E-mail: komatsu@kc.chuo-u.ac.jp; Tel: +81-3-3817-1910

Saki Batori

Saki Batori received her MSc from Chuo University, Japan, in 2025. She is currently a PhD student in the research group of Prof. Teruyuki Komatsu and a Chuo University SPRING Scholarship Awardee. Her research focuses on the development of functional biomaterials, particularly polymer-based micromotors for environmental and biomedical applications.

Teruyuki Komatsu

Teruyuki Komatsu received his PhD from Waseda University, Japan, in 1994. After postdoctoral research work at Freie Universität Berlin, Germany, as a JSPS fellow for research abroad (1995–1997), he returned to Waseda University, where he was appointed as a lecturer (1997) and was promoted to associate professor in 2003. He held the additional post of a PRESTO researcher of JST (2006–2010). Since 2010, he has been a full professor of Department of Applied Chemistry, Chuo University. His major research interests focus on synthesis and development of smart biomaterials and their practical applications.

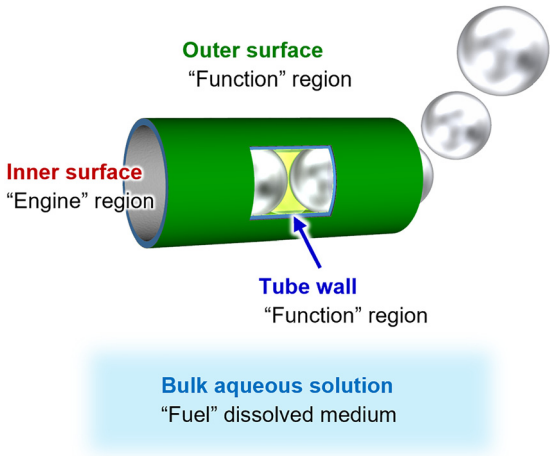

Fig. 1 Schematic of a self-propelled tubular micromotor composed of three distinct regions, each exhibiting a different functionality.

are particularly compelling because their architecture provides three spatially distinct regions—the inner surface, tube wall, and outer surface—each capable of independent functionalization (Fig. 1).[4] By assigning specific tasks to each region, multifunctional applications can be realized. Propulsion is generally driven by chemical reaction or external stimuli such as ultrasound,[5–7] magnetism,[8] and light,[9–11] with chemical reactions being particularly attractive due to the absence of electronic requirements. A common mechanism involves O_2 bubble generation *via* hydrogen peroxide (H_2O_2) disproportionation ($2H_2O_2 \rightarrow 2H_2O + O_2$), which requires immobilization of catalysts such as platinum (Pt),[12–23] silver (Ag),[24,25] manganese dioxide (MnO_2),[26–28] or catalase (Cat)[29–35] on the inner surface. The catalyst serves as the ''engine'', while H_2O_2 functions as the ''fuel''. A defining feature of micromotors is that the functionalities incorporated into the tubular walls or outer surface are amplified through autonomous propulsion. Reported applications to date include target capture and isolation,[36–43] cargo delivery,[44–50] environmental remediation and pollutant removal,[51–61] as well as (bio)sensing and assays.[62–70]

A principal goal in micromotor research is their translation into life science applications.[71–73] Potential applications include on-demand drug delivery and integration into ultra-small diagnostic or therapeutic devices. To achieve this, micromotors must accommodate bioactive macromolecules (proteins, enzymes, antibodies, nucleic acids) and biocompatible materials (polymers, liposomes, nanoparticles). However, several challenges remain to ensure safe and effective use in biological contexts. Here, we focus on ''tubular'' micromotors and provide an overview from four key perspectives.

(i) Tube wall. Traditionally, tubular walls have been fabricated *via* two primary strategies: metal thin-film roll-up nanotechnology[12,13] and template-assisted electrochemical metal deposition.[14] The former method necessitates clean-room facilities and intricate photolithography, whereas the latter employs the inner pores of polycarbonate (PC) or anodic aluminum oxide (AAO) membranes as molds, allowing for the production of uniform hollow cylinders. Consequently, template-assisted fabrication has become the prevailing method. Nevertheless, metal tubes lack biodegradability. Tubular walls composed of synthetic polymers, produced solely through polymerization, present an attractive alternative. In electrodeposition-based methods, conductive polymers such as polypyrrole, poly(3,4-ethylenedioxythiophene) (PEDOT), and polyaniline are commonly incorporated.[14,18,55,65,74] Carbon allotropes have also been explored.[75,76] However, these polymers generally exhibit poor biocompatibility. To address this, multilayered tubes composed of electrostatically stacked proteins and polyelectrolytes have been fabricated *via* layer-by-layer (LbL) assembly using porous PC membranes.[22,46] The proteinaceous tubes are fully digestible by proteases, providing high biodegradability. Nonetheless, achieving mechanically robust tubes capable of withstanding bubble ejection requires multi-step and labor-intensive procedures. In 2018, Newland *et al.* utilized porous AAO membranes to photopolymerize polyethylene glycol diacrylate, producing flexible polymer tubes.[77] Photopolymerization offers simplicity and scalability, suggesting that photocurable resins are a promising platform. By introducing negative charges onto the cylindrical wall, both the inner and outer surfaces of the liberated tubes can be modified *via* electrostatic interactions, allowing molecular designs that prioritize biofriendly nature. However, Newland's study did not extend to micromotor applications.

(ii) Engine. Biocompatibility is critical for life science applications, and this principle extends to the catalytic engine. While Pt films serve as highly effective catalysts, they are not biodegradable under physiological conditions. In contrast, small-sized Pt nanoparticles (PtNPs) are considered safe and non-cytotoxic, with applications in food and cosmetics. Recently, Escarpa *et al.* demonstrated that Prussian blue can also catalyze H_2O_2 decomposition, enabling self-propelled micromotor function.[78] Enzymatic catalysts provide even greater biocompatibility. Cat has been extensively employed as an engine due to its H_2O_2 disproportionation activity, comparable to PtNPs.[29–35] Sanchez *et al.* immobilized Cat on the inner surface of tubular micromotors, observing vigorous migration in aqueous H_2O_2 solutions.[29] Similarly, urease (Ure), which hydrolyzes urea into CO_2 and NH_3, has been used as an engine, enabling slow propulsion in urea solutions without bubble formation.[79–81] Because gas bubbles do not accumulate, Ure-powered micromotors are compatible with living organisms and obviate the need for surfactants, which can disrupt cell membranes and protein structures.[82,83] A notable feature of enzyme-powered micromotors is that the swimming velocity depends on catalytic activity, with maximum speeds achieved at the enzyme's optimal temperature and pH.[29–32,34] Consequently, velocity can be modulated by environmental conditions, and precise control using external stimuli (*e.g.*, light) enables dynamic manipulation of micromotor propulsion.

(iii) Fuel. Most micromotors are propelled in 1–10% w/v H_2O_2 solutions *via* O_2 bubble generation. H_2O_2, however, is a strong oxidant that can damage cell membranes and induce cytotoxicity, as well as compromise protein and enzyme structure and function. Thus, biological applications have historically been limited to specific contexts and durations. Alternative fuels are being explored for broader applicability.

For instance, Feringa *et al.* developed glucose-fueled micromotors using glucose oxidase (GOD) and Cat as the engine.[84] GOD oxidizes glucose to generate H_2O_2, which Cat subsequently decomposes to produce O_2. A complication of this system is that O_2 is required to sustain the conversion of glucose by GOD.

H_2 bubble-powered micromotors have also been reported. Wang *et al.* utilized strong acids (HCl or gastric acid) as a fuel and zinc (Zn) metal as the engine, generating thrust through the redox reaction $Zn(s) + 2H^+(aq) \rightarrow Zn^{2+}(aq) + H_2(g)$.[85] *In vivo* application was demonstrated in the mouse stomach.[86,87] Magnesium (Mg)-driven micromotors coated with enteric polymer similarly enabled localized drug release in the gastrointestinal tract.[88] More recently, metal–organic framework (MOF)-based Zn-driven tubes have been developed for sustained cargo release.[89] Sodium borohydride ($NaBH_4$) with Pt or palladium (Pd) engines has also been employed to generate H_2 bubbles,[90] though instability of $NaBH_4$ in a neutral pH limits its practicality. Ure-powered micromotors utilizing urea as a fuel operate at physiologically relevant concentrations (human blood: 2.1–7.1 mM; urine: 127–698 mM),[91,92] demonstrating promising applicability in biological systems.

(iv) Drug loading. The application of tubular micromotors as active drug delivery systems has attracted considerable interest. Micromotors can transport therapeutic agents to targeted sites and release them locally, enhancing treatment efficacy while minimizing side effects. Existing tube micromotors typically exhibit low drug-loading capacity, as drugs are immobilized *via* electrostatic interactions, π–π stacking, or hydrophobic interactions.[46–48] Liposomes, spherical vesicles composed of phospholipid bilayers, offer a promising strategy to increase payload capacity. Dense adsorption of drug-encapsulated liposomes onto micromotor surfaces could dramatically enhance the transport efficiency. To date, tubular micromotors incorporating liposomes on their exterior have not been reported.

Guided by these four design principles, we have developed photocurable polymer tube micromotors. This review summarizes recent findings concerning their synthesis, structural features, and functional properties. Hollow acrylic-resin cylinders were fabricated *via* in-template photopolymerization, engine molecules were immobilized on the inner surface, and the desired proteins and liposomes were attached to the outer surface (Scheme 1). The swimming velocity of Cat-driven tubes can be modulated by visible light irradiation. Notably, Pt tubes powered by H_2 bubbles enable the capture of live cells in H_2O_2-free environments. Furthermore, micromotors loaded with anticancer drug-encapsulated liposomes efficiently induce cell death upon near-infrared (NIR) irradiation. Photocurable polymer tube micromotors represent a highly scalable, ultra-small platform with substantial potential for life science applications.

2. Photocurable polymer tube micromotors with a PtNP interior

2.1. Synthesis and self-propulsion behavior of Pt tubes

Representative acrylic-resin-based tubular micromotors possessing PtNP-lined interiors (Pt tubes) were fabricated *via* a two-step template synthesis employing track-etched PC membranes (pore size: 8.0 μm) (Scheme 1B).[93] The procedure comprised: (i) photopolymerization to generate polymeric tube precursors, followed by (ii) LbL deposition to construct an intermediate magnetite nanoparticle (MNP) layer and an innermost PtNP catalytic layer. Cross-linked acrylic resin, poly[bis{2-(methacryloyloxy)ethyl}phosphate] (PBMP), was selected as the wall material (Scheme 1A) owing to its mechanical robustness and negatively charged phosphate groups, which permit subsequent electrostatic LbL assembly on both tubular surfaces. A methanol solution of BMP monomer was introduced into the microporous PC membrane and photopolymerized under a N_2 atmosphere with ultraviolet (UV, 365 nm) irradiation. For LbL modification of the interior wall, the polymer-embedded PC membrane was mounted in a stainless-steel holder, and sequential pressure filtrations of aqueous dispersions of MNPs, poly(L-arginine) (PLA, a cationic adhesive), and PtNPs were carried out. This yielded PBMP/MNP/PLA/PtNP assemblies (Pt tubes) within the membrane pores.[93] Dissolution of the PC template followed by freeze-drying of the residues produced a black powder of Pt tubes.

Scanning electron microscopy (SEM) revealed uniform hollow cylinders with an outer diameter of 7.6 ± 0.3 μm, a wall thickness of 284 ± 26 nm, and a tube length of 18.3 ± 0.3 μm (Fig. 2A). Dispersions of lyophilized Pt tubes were prepared by brief sonication in phosphate buffer (PB, pH 7.0). Upon addition of H_2O_2, the Pt tubes exhibited vigorous motility through the continuous expulsion of O_2 bubbles, with an average velocity of 305 ± 63 μm s^{-1} at [H_2O_2] = 2% w/v (Fig. 2B).[93] Most tubes swam with a rotational trajectory due to slight curvature along their longitudinal axis. Introduction of a neodymium (Nd)–magnet enabled precise control of the swimming direction, propelling the tubes toward the magnetic field as a result of the MNP layer. The swimming velocity was dependent on H_2O_2 concentration (1–4% w/v), with increased bubble ejection frequency accelerating motility (Fig. 2C).

2.2. Capture of targets by protein-coated Pt tube micromotors

Functionalization of the external surface of the Pt tubes with proteins endows them with specialized recognition capabilities. As an initial demonstration, avidin (Avi), a tetrameric protein with exceptionally strong affinity for biotin, was employed. Given that Avi is a basic protein with an isoelectric point of 10–10.5, Avi-functionalized Pt tubes (Avi/Pt tubes) were readily prepared by simple immersion of negatively charged Pt tubes in aqueous Avi solution (Scheme 1B).[93] The motility of the Avi/Pt tubes in H_2O_2 solution was essentially indistinguishable from that of unmodified Pt tubes. To assess their recognition capability, biotinylated fluorescein (bFL) was employed as a model target. Self-propelled Avi/Pt tubes captured bFL far more efficiently than static, non-motile controls.

Avi/Pt tubes retained motility within confined spaces, such as the narrow microchannel (0.4 mm width, 0.1 mm depth) of a microfluidic chip (Fig. 2D). Upon injection at the entrance reservoir [position (1)], the swimming tubes were magnetically guided to the exit reservoir [position (3)] through the

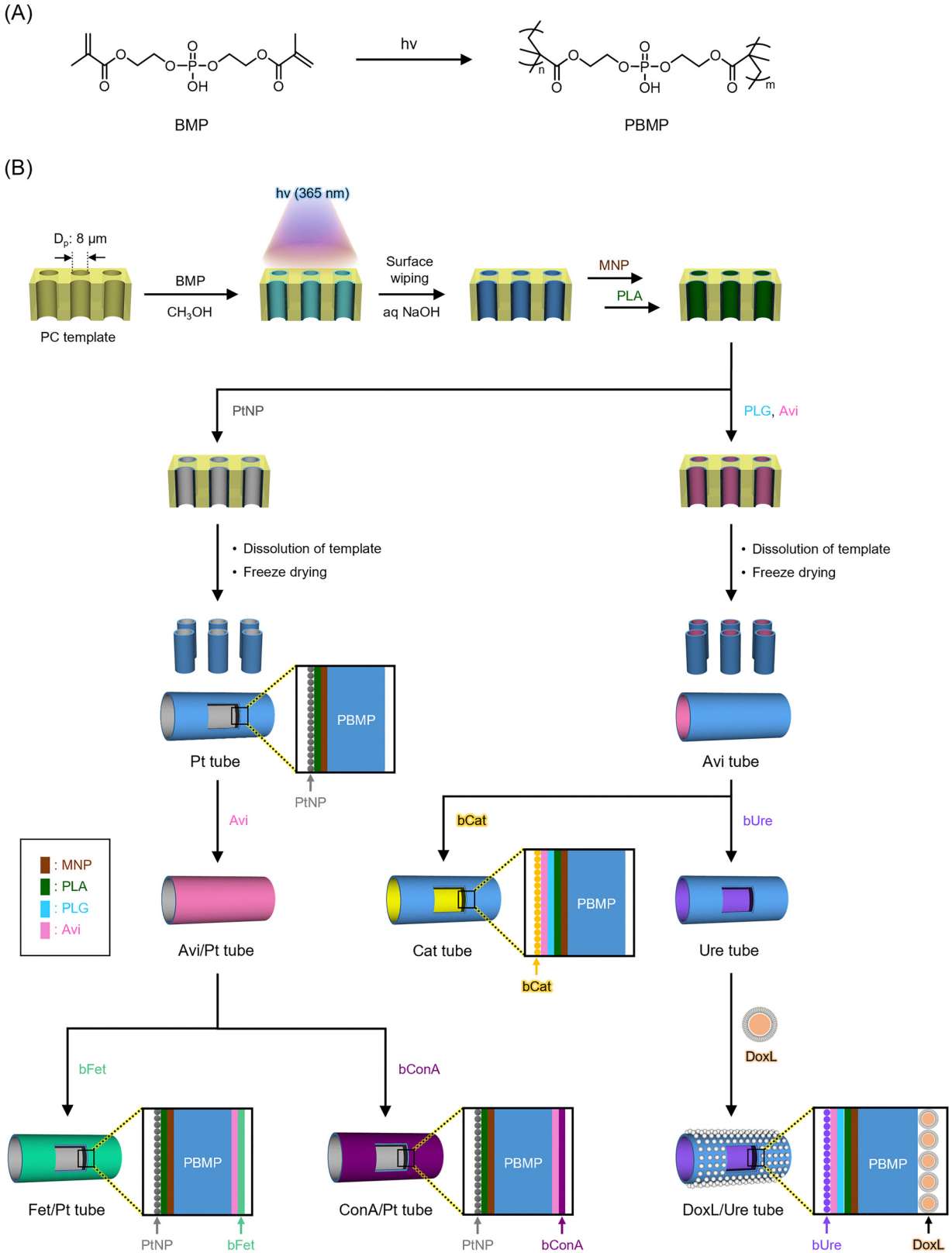

Scheme 1 (A) Polymerization of BMP to yield PBMP. (B) Synthetic scheme of photocurable polymer-based tubes *via* photopolymerization and LbL deposition in a track-etched PC membrane template, followed by outer-surface coating. Structures include: PBMP/MNP/PLA/PtNP tube (Pt tube), Avi/PBMP/MNP/PLA/PtNP tube (Avi/Pt tube), bFet-Avi/PBMP/MNP/PLA/PtNP tube (Fet/Pt tube), bConA-Avi/PBMP/MNP/PLA/PtNP tube (ConA/Pt tube), PBMP/MNP/PLA/PLG/Avi tube (Avi tube), PBMP/MNP/PLA/PLG/Avi-bCat tube (Cat tube), PBMP/MNP/PLA/PLG/Avi-bUre tube (Ure tube), and DoxL/PBMP/MNP/PLA/PLG/Avi-bUre tube (DoxL/Ure tube) (ref. 93, 96, 105 and 106).

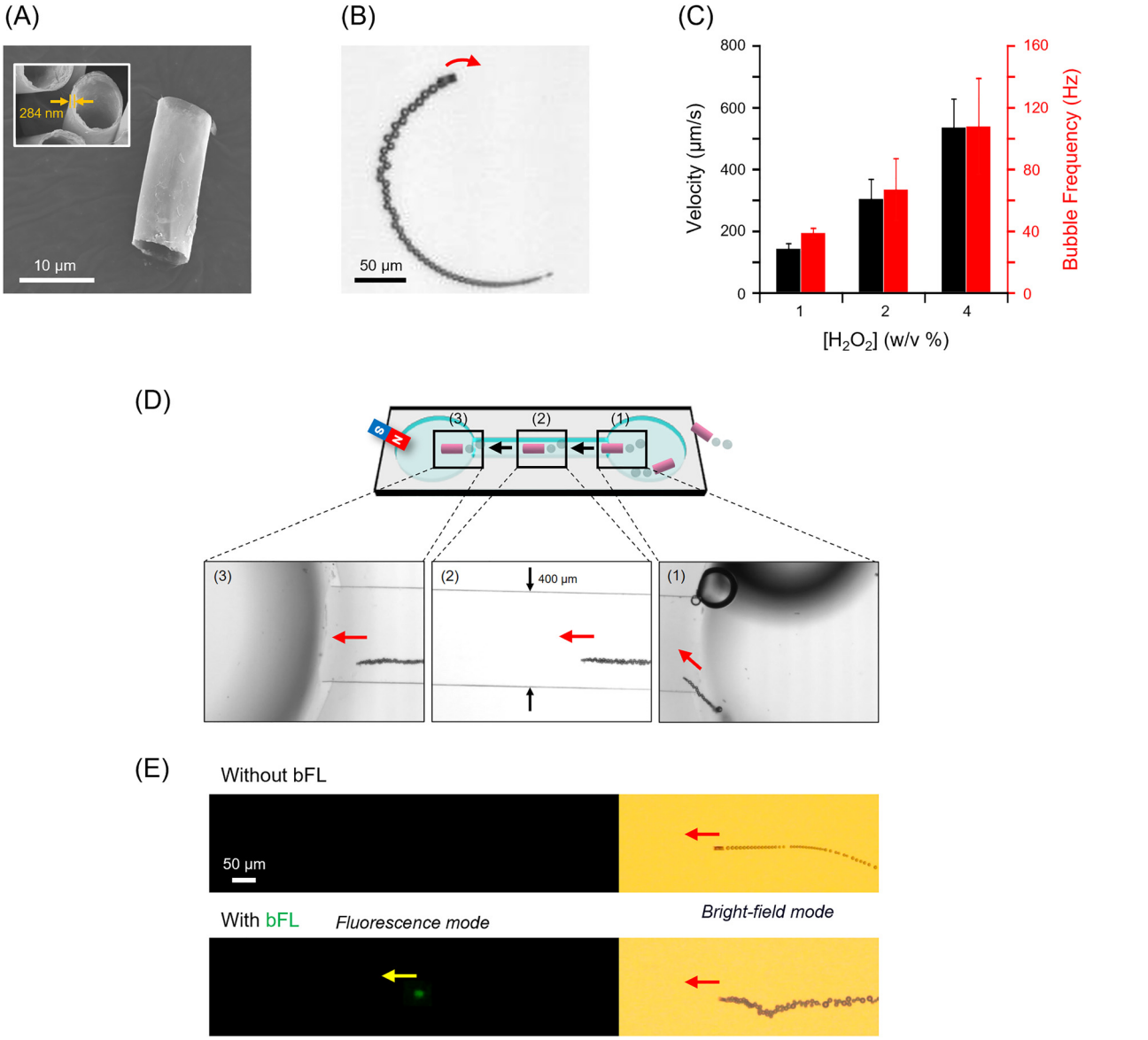

Fig. 2 (A) SEM images of Pt tubes. (B) Microscopic observation of Pt tube micromotors powered by O_2 bubble ejection in PB solution (2% w/v H_2O_2, 0.2% w/v Triton-X 100). (C) Relationship between the velocity of Pt tube micromotors and H_2O_2 concentration in PB solution (0.2% w/v Triton-X 100). (D) Microscopic observation of an Avi/Pt tube micromotor in PB solution (2% w/v, H_2O_2, 0.2% w/v Triton-X 100) in a microfluidic channel. The micromotor was magnetically guided from position (1) to (3) using an Nd magnet. (E) Microscopic observations of Avi/Pt tube micromotors in PB solution (2% w/v H_2O_2, 0.2% w/v Triton-X 100) in a microfluidic channel under a magnetic field: (upper) without bFL, (lower) with bFL. Right, bright-field mode; left, fluorescence mode. From ref. 93. Copyright 2024, American Chemical Society.

microchannel. Fluorescence microscopy readily distinguished micromotors bearing bFL (bright) from those without (dark) (Fig. 2E). This demonstrated that Avi/Pt tubes can detect and visualize biotinylated targets in dilute and trace samples (5 nM, 10 μL). Antibody-coated tubular micromotors hold considerable promise for detecting minute quantities of antigens across diverse microchip-based diagnostic platforms.

A subsequent challenge involved capturing influenza virus particles. Viral infection is initiated by binding of the surface glycoprotein hemagglutinin (HA) to sialylated glycans. Fetuin (Fet), a glycoprotein from fetal bovine serum, contains tri-branched *N*-acetylneuraminic acid-terminated oligosaccharides that bind to HA. Accordingly, biotinylated Fet (bFet) was immobilized on Avi/Pt tubes (Scheme 1B). The resulting Fet/Pt tubes exhibited self-propulsion in H_2O_2 solution with an average velocity of 320 ± 84 μm s^{-1}.

To establish a model system, HA-bound fluorescent nanoparticles (HA-FNPs, 100 nm diameter) were prepared as pseudo-influenza A virus particles (Fig. 3A).[93,94] These non-infectious, luminous particles are easily handled under standard laboratory conditions and can be sensitively monitored with conventional fluorometric techniques. Each nanoparticle displayed approximately 350 HA molecules, a density comparable to natural influenza A virus.[95] Cryogenic transmission electron

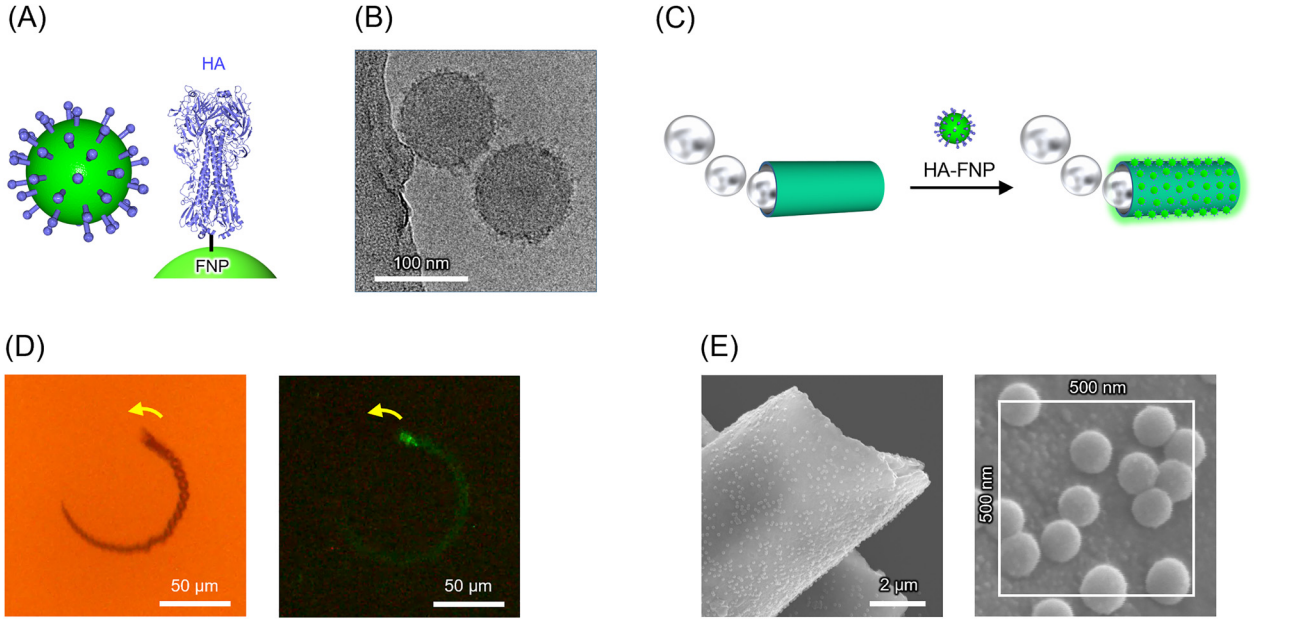

Fig. 3 (A) Structural model of HA-FNP. (B) Cryo-TEM image of HA-FNP. (C) Schematic illustration of HA-FNP capture by a Fet/Pt tube micromotor. (D) Microscopic observations of HA-FNP-Fet/Pt tube micromotors in PB solution (2% w/v H_2O_2, 0.2% w/v Triton-X 100): left, bright-field mode; right, fluorescence mode. (E) SEM images of HA-FNP-bound Fet/Pt tubes. From ref. 93. Copyright 2024, American Chemical Society.

microscopy (cryo-TEM) confirmed a spiky HA-coated surface (Fig. 3B).

Introduction of HA-FNPs into dispersions of swimming Fet/Pt tubes resulted in immediate green fluorescence emission from the tubes, confirming the binding of pseudo-viral particles on their exterior surfaces (Fig. 3C and D).[93] The swimming velocity (286 ± 70 μm s^{-1}) was nearly identical to that of unmodified Fet/Pt tubes. Fluorescence quantification indicated an average of 2.3 × 10^4 HA-FNPs bound per tube, consistent with SEM observations of ~2.0 × 10^4 particles per tube (Fig. 3E). These results establish that Fet-functionalized micromotors specifically recognize HA-bearing viral surfaces. Thus, Fe/Pt tubes represent a promising platform for the selective removal and separation of influenza A virus particles at the microscale.

3. Photocurable polymer tube micromotors with a Cat interior

3.1. Synthesis and self-propulsion behavior of the Cat tubes

Nanoscale PtNP-based engines demonstrate acceptable safety, while biocatalytic enzyme-driven engines offer even greater biocompatibility. Cat is a hemoprotein enzyme capable of decomposing H_2O_2 with high efficiency. Acrylic-resin tube micromotors with Cat on the internal surface (Cat tubes) were synthesized by immobilizing biotinylated Cat (bCat) on the inner surface of tubes bearing an Avi interior (Avi tubes) (Scheme 1B).[96] Upon addition of H_2O_2 to the Cat tubes dispersion, the tubes exhibited self-propulsion through the expulsion of O_2 bubbles (Fig. 4A). The average velocity was 130 ± 35 μm s^{-1} (pH 7.0, [H_2O_2] = 2% w/v 25 °C). Notably, the motion speed of the Cat tubes exceeded that of the previously reported Cat-driven tubular micromotor.[30,31,34,35]

The enzyme activity significantly influenced the mobility of the Cat tubes.[29–32,34] Both pH and temperature are critical factors governing enzyme performance. As expected, the swimming speed of the Cat tubes varied with pH, reaching a maximum of 128 ± 10 μm s^{-1} at pH 7.0 (25 °C), the optimal pH for Cat (Fig. 4B).[97] Furthermore, at constant pH 7.0, the tubes exhibited the highest velocity (241 ± 38 μm s^{-1}) at 35 °C, close to the optimal temperature (37 °C) for Cat (Fig. 4C). The addition of sodium azide (NaN_3), a Cat inhibitor, led to the cessation of autonomous motion within 1 min ([NaN_3] = 25 μM). Because N_3^- coordinates to the ferric heme of Cat and inhibits enzyme activity, measuring the time until Cat tubes ceased movement allowed estimation of the NaN_3 concentration, suggesting potential application as a detection device.

3.2. Velocity control of Cat tube micromotors using light irradiation

Controlling micromotor velocity with external stimuli, particularly light, is of great interest. Several researchers have demonstrated that tubular micromotor speed can be modulated by irradiation with NIR, visible, and UV light.[98–100] Notably, we found that Cat tubes swam faster (270 ± 43 μm s^{-1}) under visible light irradiation (460–495 nm) (Fig. 4D). Termination of light exposure caused an instantaneous decrease in motion speed, which returned to the baseline level. The frequency of bubble ejection increased from 30 bubbles per s before light irradiation to 45 bubbles per s during irradiation. The velocity increased proportionally with light intensity (Fig. 4E). In other words, the swimming speed of the Cat tubes directly reflected the intensity of visible light. Importantly, visible light irradiation did not affect the velocity of Cat tubes lacking MNPs. This demonstrated that photoinduced control of motion was only

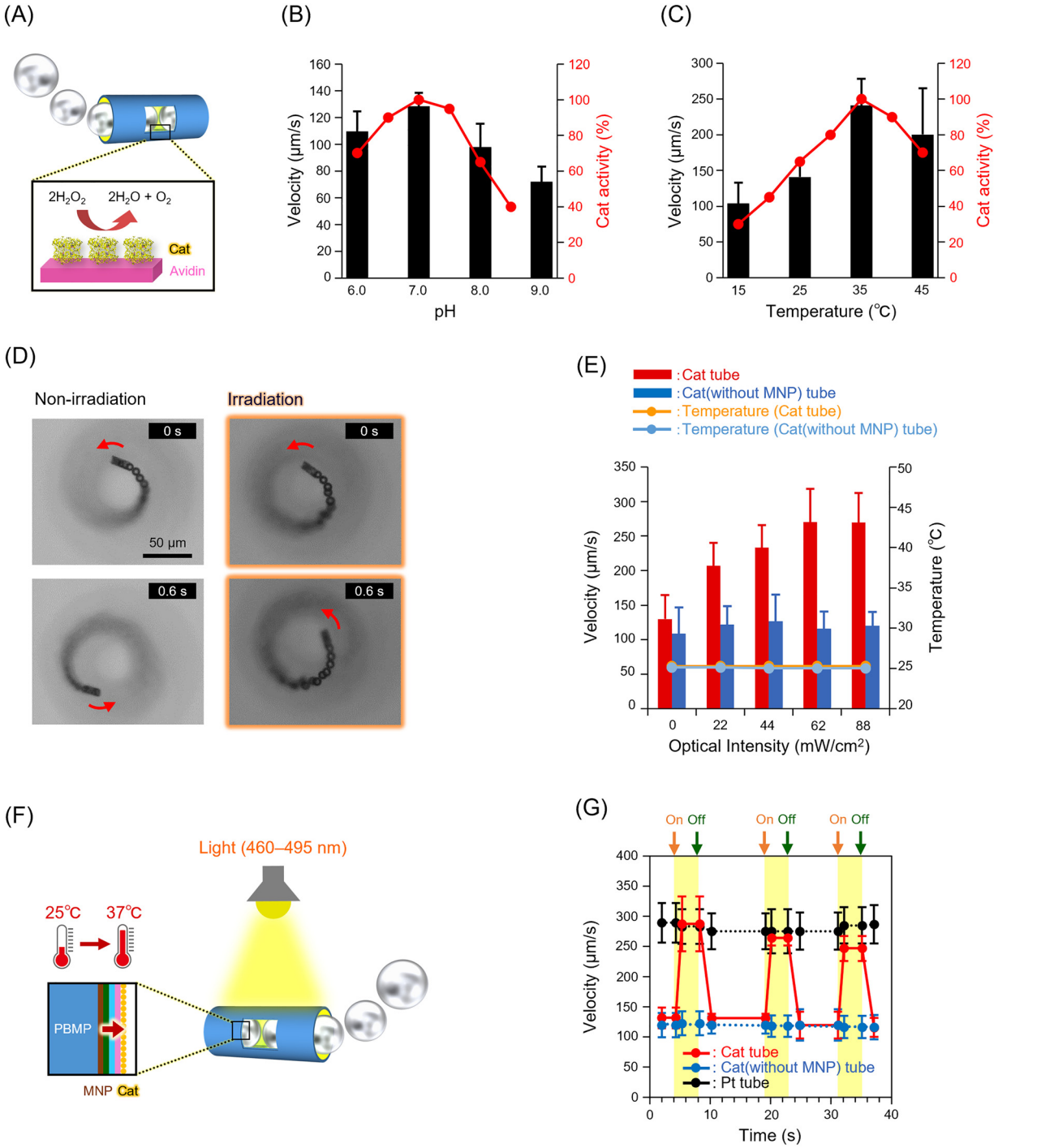

Fig. 4 (A) Schematic illustration of a Cat tube micromotor powered by O_2 bubble ejection. (B) Effect of pH on the average velocity of Cat tube micromotors (2% w/v H_2O_2, 0.1% w/v Triton X-100) and Cat activity[97] at 25 °C. (C) Effect of temperature on the average velocity of Cat tube micromotors (2% w/v H_2O_2, 0.1% w/v Triton X-100) and Cat activity[97] at pH 7.0. (D) Microscopic observation of Cat tube micromotors in PB solution (2% w/v H_2O_2, 0.1% w/v Triton-X 100); left, without light irradiation; right, under light irradiation. (E) Effect of optical intensity on the average velocity of Cat tube micromotors (2% w/v H_2O_2, 0.1% w/v Triton X-100) and on bulk solution temperature. (F) Schematic illustration of wall heating in a Cat tube micromotor under visible light irradiation. (G) Relationship between micromotor velocity and repeated light on/off cycles in PB solution (2% w/v H_2O_2, 0.1% w/v Triton-X 100). From ref. 96. Copyright 2024, American Chemical Society.

achievable in Cat tubes containing both MNP and Cat layers. Various experiments revealed that the observed speed increase was attributable to the photothermal effect of MNPs in the wall (Fig. 4F).[96] Shi *et al.* reported that MNPs exhibit higher photothermal heating efficiency under white-light illumination compared to NIR irradiation.[101] The bulk aqueous solution remained

at 25–26 °C under irradiation, indicating that local photothermal heating of the tube wall by MNPs enhanced the activity of adjacent Cat enzymes (Fig. 4F). Because the maximum swimming velocity was achieved as light intensities of 62–88 mW cm^{-2}, the inner wall of the tube is presumed to reach the optimal temperature for Cat (37 °C) within this range. Acceleration and deceleration of the Cat tubes were repeatedly observed upon switching the light on and off, with rapid response times (Fig. 4D and G).[96] Upon light irradiation, maximum speed was reached within 1 s; upon cessation, the velocity returned to the baseline within 3 s. By contrast, repetitive irradiation of Cat tubes without MNPs and of Pt tubes did not produce velocity changes (Fig. 4G). The remarkable on–off light responsiveness of the Cat tubes highlights their potential for expanding the scope of micromotor applications.

4. Pt tube micromotors powered by H_2 bubbles in NH_3BH_3 solution

4.1. Self-propulsion behavior of Pt tubes and survival of *E. coli* in NH_3BH_3 solution

H_2O_2 has been the most frequently used fuel for micromotors. However, the strong oxidizing nature of H_2O_2 limits its applications, particularly due to rapid inactivation of live cells. A major challenge in the development of micromotor is ensuring that the fuel does not adversely affect living organisms. Micromotors powered by gas bubbles without reliance on H_2O_2 would therefore offer significant advantages across various fields. Ammonia borane (NH_3BH_3) is a promising H_2 source owing to its high hydrogen content, water solubility, nontoxicity, and stability.[102] The hydrolysis of NH_3BH_3 on Pt catalysts generates H_2 gas under ambient conditions ($NH_3BH_3 + 2H_2O \rightarrow 3H_2 + NH_4^+ + BO_2^-$).[103,104] In 2024, we found that Pt tubes exhibited vigorous self-propulsion in aqueous NH_3BH_3 solution, driven by the ejection of H_2 gas bubbles from the terminal opening, with an average speed of 103 ± 24 μm s^{-1} ([NH_3BH_3] = 0.6 M) (Fig. 5A).[105] The velocity of the micromotors and the frequency of H_2 bubble generation increased with NH_3BH_3 concentration. The PtNP layer functioned as a catalyst for NH_3BH_3 hydrolysis, thereby powering micromotor movement.

To date, several tubular micromotors capable of capturing *E. coli*—a model bacterial target—have been reported. In these studies, tube surfaces were functionalized with the lectin concanavalin A (ConA), which specifically binds to terminal carbohydrates of lipopolysaccharides (LPS) on bacterial outer membranes. Wang *et al.* demonstrated bacterial isolation using ConA-modified tube micromotors in 7.5% w/v H_2O_2 solution, although quantitative evaluations were not conducted.[38] Similarly, we developed ConA-wrapped protein tube micromotors capable of binding *E. coli* in aqueous 2% w/v H_2O_2.[35] However, in both cases, most bacterial cells became non-viable and non-culturable due to the potent oxidative effects of H_2O_2.

To evaluate whether *E. coli* could survive in aqueous NH_3BH_3, we employed a genetically engineered GFP-expressing *E. coli* (GFP: green fluorescent protein). The bacteria maintained fluorescence in HEPES buffer containing 0.6 M NH_3BH_3 and were successfully cultured on LB agar plates even after exposure to the same solution.[105] Clear colony formation was observed after 16 h, confirming bacterial survival. In contrast, *E. coli* exposed to 2% w/v H_2O_2 showed no colony formation after 16 h. This stark contrast highlights NH_3BH_3 as a safer fuel alternative for micromotors in life science applications.

4.2. Capture of *E. coli* by ConA/Pt tube micromotors

ConA/Pt tubes were fabricated by immersing Avi/Pt tubes in biotinylated ConA (bConA) solution (Scheme 1B). Upon addition of *E. coli* to an NH_3BH_3 dispersion containing swimming ConA/Pt tubes, the tubes efficiently captured the bacteria (Fig. 5B).[105] Fluorescence microscopy clearly showed *E. coli* binding to ConA/Pt tube micromotors (Fig. 5C). A single treatment removed 79% of bacteria from the dispersion (Fig. 5D).[105] The capture efficiency was significantly higher than those of swimming PSS/Pt tubes [PSS, poly(styrene sulfonate)] and non-swimming ConA/PLG tubes [PLG, poly(L-glutamic acid)], indicating that (i) specific binding between ConA and bacterial LPS mediated capture, and (ii) autonomous propulsion enhanced collision frequency, thereby improving efficiency relative to non-motile counterparts. On average, 5.5 *E. coli* cells adhered to each tube. Confocal laser scanning microscopy (CLSM) slice images of *E. coli*-bound ConA/Pt tubes confirmed approximately six bacteria attached per tube (Fig. 5E).

A small volume of the supernatant was spread onto LB agar plate and incubated at 37 °C. The colony incidence rate for the ConA/Pt tube group was 23% compared to the reference group (identically treated *E. coli* without tubes) (Fig. 5F), consistent with residual cell rates determined by fluorescence (Fig. 5D).[105] By contrast, when the same experiment was performed in 2% w/v H_2O_2 solution, no colony formation occurred, indicating complete bacterial death. These results demonstrate that self-propelled ConA/Pt tubes can efficiently capture live *E. coli* in NH_3BH_3 solution. Thus, NH_3BH_3 enables the development of tubular micromotors targeting live cells in environments that preserve cellular viability.

5. Photocurable polymer tube micromotors with a Ure interior and drug-loaded liposome exterior

5.1. Synthesis and self-propulsion behavior of DoxL/Ure tubes

Active drug delivery using tubular micromotors capable of autonomous propulsion under physiological conditions has attracted considerable attention.[46–50] The Ure-engine catalyzes the hydrolysis of urea, generating a mechanical driving force without bubble formation. Several studies have investigated Ure-powered tubular micromotors.[79–81]

Doxorubicin (Dox), an anthracycline antibiotic, is clinically used in liposomal formulations. In 2025, we synthesized DoxL/Ure tubes by sequentially immersing Avi tubes in (i) a biotinylated Ure (bUre) solution and (ii) a phospholipid liposome dispersion containing Dox (DoxL; diameter 148 nm, encapsulating ~1.6×10^{-19} mol of Dox per liposome) and a fluorescent

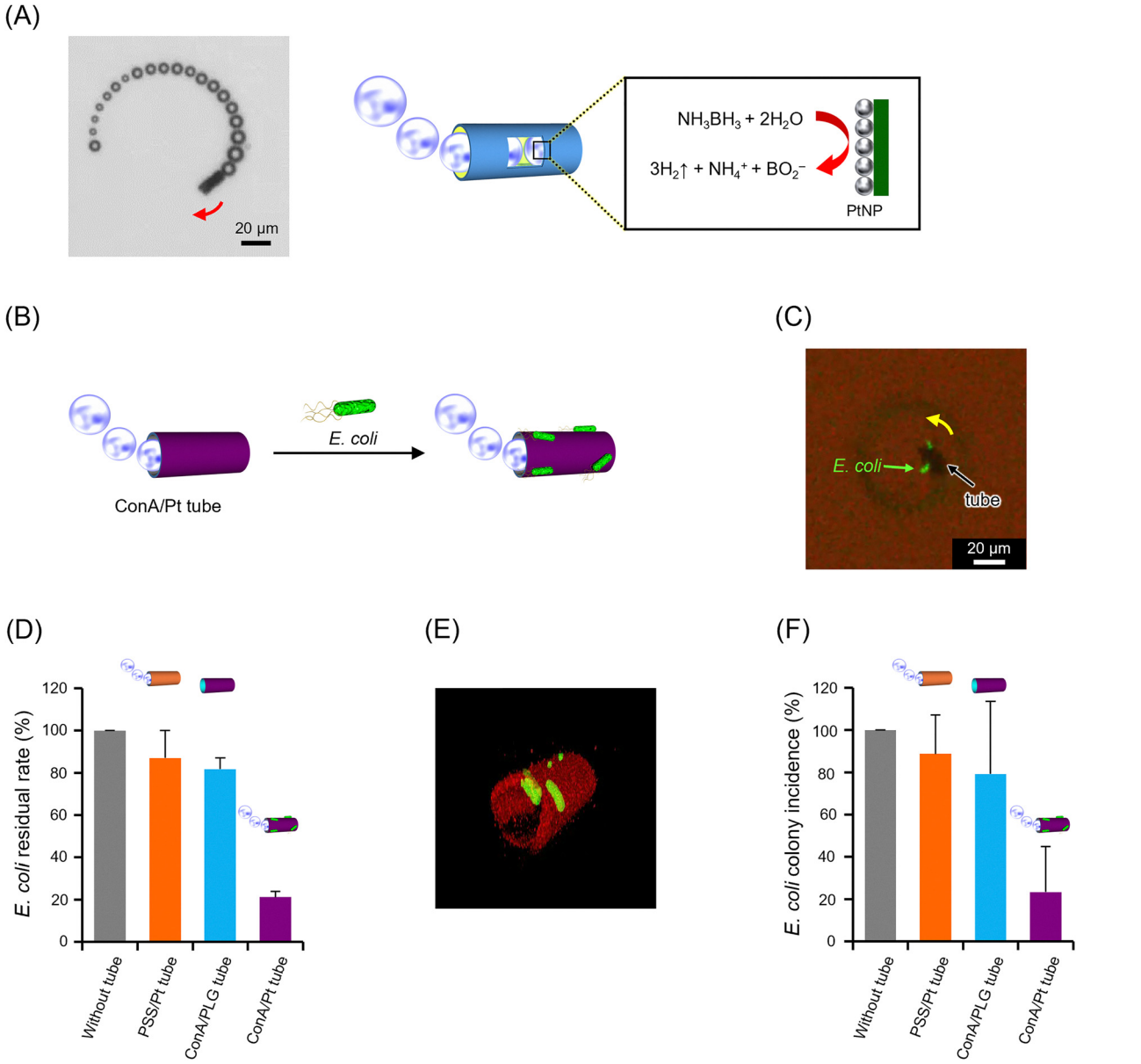

Fig. 5 (A) Microscopic observation and schematic illustration of a Pt tube micromotor powered by H_2 bubble ejection in PB solution (pH 7.0, 0.6 M NH_3BH_3, 0.2% w/v Triton X-100). (B) Schematic illustration of *E. coli* capture by a ConA/Pt tube micromotor. (C) Microscopic observation of the *E. coli*-bound ConA/Pt tube micromotor in HEPES buffer (pH 6.8, 0.6 M NH_3BH_3, 0.2% w/v Triton X-100). (D) *E. coli* residual rate after treatment with ConA/Pt tube micromotors determined by fluorescence measurements. (E) 3D reconstruction from CLSM slice images of an *E. coli*-bound ConA/Pt tube. *E. coli*, green; PBMP wall stained with tetramethylrhodamine methyl ester, red. (F) *E. coli* colony incidence after treatment with ConA/Pt tube micromotors. From ref. 105. Copyright 2024, American Chemical Society.

probe [1,1′-dioctadecyl-3,3,3′,3′-tetramethylindodicarbocyanine (DiD)] (Scheme 1B).[106] SEM images confirmed the immobilization of DoxL on the tube surface (Fig. 6A). The exterior of the DoxL/Ure tube appeared markedly rougher than that of the smooth Ure tube, indicative of high-density DoxL adsorption. The number of DoxL particles absorbed per Ure tube was estimated at $\sim 2.5 \times 10^4$, corresponding to a surface coverage of 93%. This equates to $\sim 4.0 \times 10^{-15}$ mol of Dox per tube, 69-fold greater than that reported for Pumera's tube micromotors, which relied on electrostatic interactions for drug loading.[48] Thus, DoxL/Ure micromotors are capable of transporting chemotherapeutic agents at exceptionally high concentrations and densities. CLSM images of the DoxL/FUre (FUre: fluorescein-labeled bUre) tube exhibited strong fluorescence from both fluorescein (tube wall) and DiD (liposome), confirming successful immobilization of FUre on the Avi layer and adsorption of DoxL onto the tube exterior (Fig. 6B).

DoxL/Ure tubes exhibited autonomous propulsion in PBS containing a physiological concentration of urea (Fig. 6C).[106] The average velocity was 11.4 ± 2.5 μm s^{-1} ([urea] = 100 mM), exceeding previously reported values for Ure-powered tube micromotors.[79–81] Within the tubular cavity, Ure catalyzes the

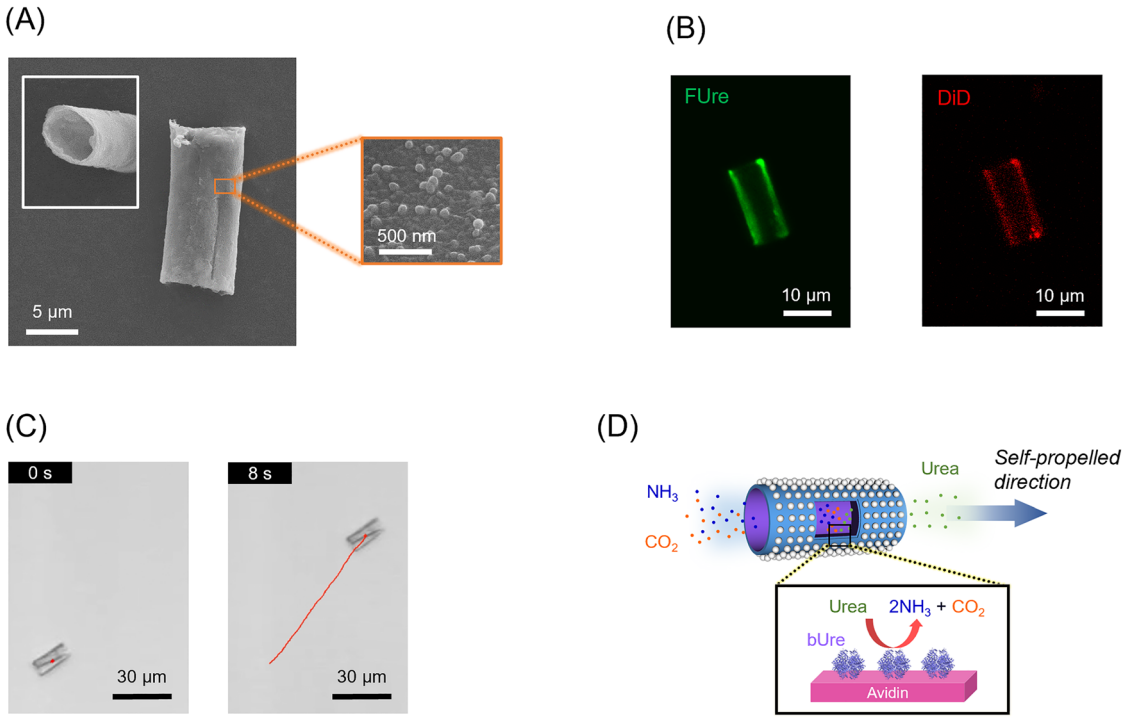

Fig. 6 (A) SEM images of DoxL/Ure tubes. (B) CLSM images of DoxL/FUre tubes. Green fluorescence: FUre; red fluorescence: DiD. (C) Microscopic observation of a DoxL/Ure tube micromotor with trajectory in PBS solution ([urea] = 100 mM). (D) Schematic illustration of DoxL/Ure tube micromotor propulsion *via* urea decomposition into NH_3 and CO_2. From ref. 106. Copyright 2025, American Chemical Society.

decomposition of urea into CO_2 and NH_3, which are subsequently converted into ionic species such as NH_4^+, HCO_3^-, CO_3^{2-}, and OH^- (Fig. 6D). The resulting ionic concentration gradient drives outward fluid diffusion, generating internal flow that propels the micromotor in the opposite direction.[79–81]

5.2. Drug release capacity and anticancer activity of DoxL/Ure tube micromotors

DoxL immobilized onto the tube surface undergoes a gel-to-liquid crystalline phase transition at 38.5 °C (T_c). For externally triggered drug release, NIR irradiation (1490 nm) was applied to heat the DoxL/Ure tube dispersion. After 2 min of irradiation, the solution temperature exceeded T_c, reaching 39 °C, and 76.4% of the encapsulated Dox was released within 5 min (Fig. 7A). These results demonstrate that NIR irradiation effectively triggers drug release from the DoxL/Ure tubes, highlighting their potential for remote-controlled cancer therapy.

The cytotoxicity of the DoxL/Ure tubes was evaluated in MCF-7 breast cancer cells. Treatment with the DoxL/Ure micromotor reduced cell viability to 19 ± 4%, a remarkable decrease compared with the non-swimming control group (Fig. 7B).[106] The autonomous propulsion enhances micromotor–cell interactions, promoting electrostatic adhesion to cell membranes. The cationic liposomes of the DoxL/Ure tubes facilitate adhesion during swimming, and subsequent NIR-induced heating triggers localized Dox release at the cell surfaces. This delivers a high concentration of the drug directly to cells, resulting in effective cytotoxicity (Fig. 7C).

To validate this mechanism, CLSM was used to monitor MCF-7 cells incubated with DoxL/Ure tube micromotors (Fig. 7D).[106] Without NIR irradiation, DiD (liposome membrane) and Dox (liposome core) fluorescence were observed on the tube surface. Upon NIR exposure, Dox fluorescence appeared in the cytoplasm, indicating successful release and cellular uptake, whereas DiD fluorescence remained confined to the tube, implying that only Dox was delivered. Thus, self-propelled DoxL/Ure tubes carrying high drug payloads can adhere to cancer cells and enable on-demand drug release under light irradiation, resulting in potent anticancer activity. Given the versatility of liposomal drug encapsulation, tubular micromotors represent a promising platform for active targeted drug delivery across diverse biomedical applications.

6. Conclusion and prospects

By combining photopolymerization within a porous PC template with LbL assembly, a wide variety of acrylic-resin-based tubular micromotors can be fabricated. Tubes bearing PtNPs on their inner surfaces autonomously swim in aqueous H_2O_2 and NH_3BH_3 solutions by ejecting O_2 and H_2 bubbles, respectively. Notably, we discovered that NH_3BH_3 serves as a fuel for H_2 gas release, enabling self-propulsion. Functionalities introduced onto the outer surface are amplified by autonomous locomotion. For example, Pt tube micromotors wrapped with Fet captured influenza virus-shaped nanoparticles, suggesting

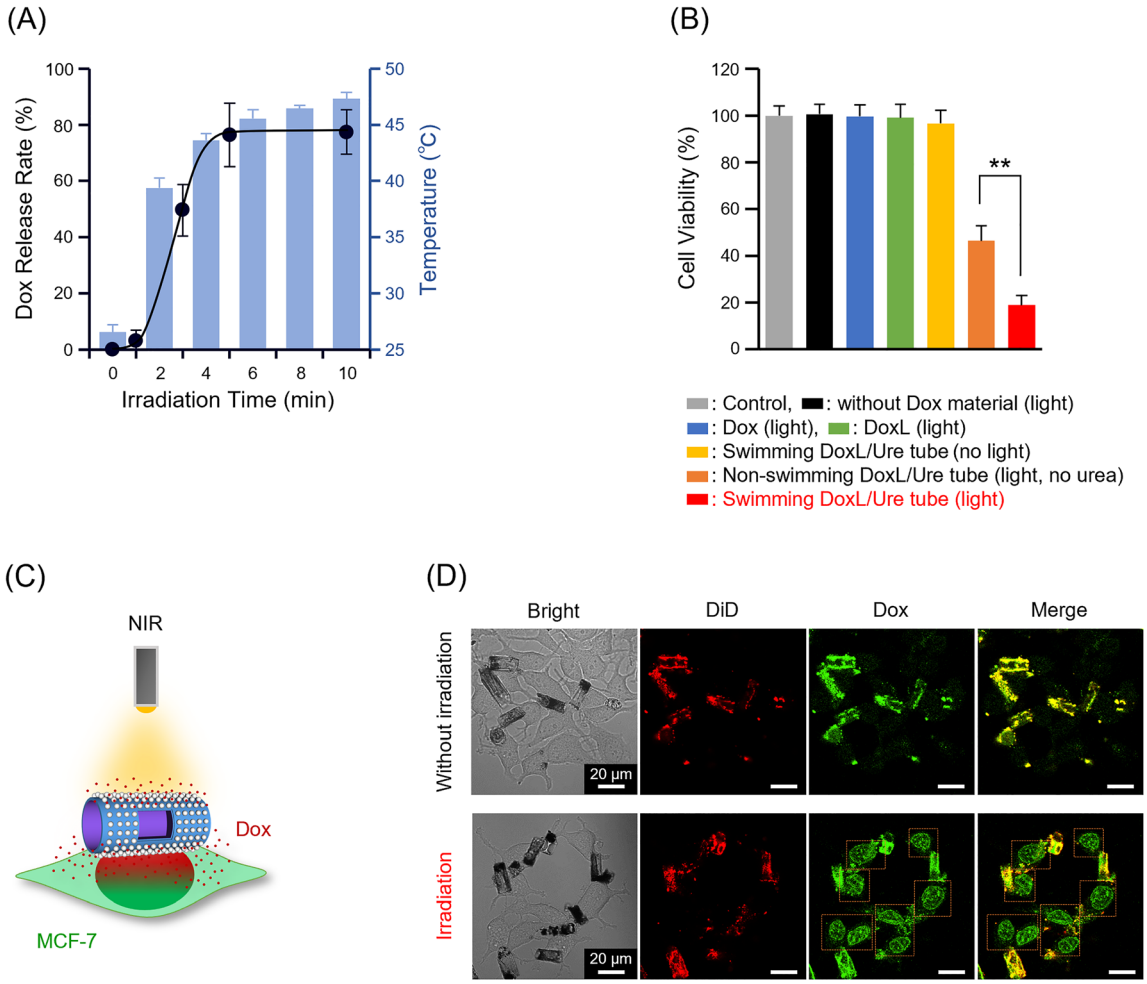

Fig. 7 (A) Relationships between NIR irradiation time and (left axis) Dox release rate from DoxL/Ure tubes and (right axis) bulk solution temperature. (B) Viability of MCF-7 cells after treatment with DoxL/Ure tube micromotors, washing, and NIR laser irradiation (1490 nm), determined by CCK-8 assay. Control group: no urea, no Dox, no light irradiation. $^{**}p < 0.01$ *vs.* the non-swimming DoxL/Ure tube group (light, no urea). (C) Schematic illustration of NIR-induced DoxL release from a DoxL/Ure tube micromotor bound to MCF-7 cells. (D) CLSM images of MCF-7 cells after incubation with DoxL/Ure tube micromotors, washing, and NIR irradiation. Red fluorescence: DiD; green fluorescence: Dox. From ref. 106. Copyright 2025, American Chemical Society.

potential as detectors for viral infections. The swimming speed of Cat-powered micromotors was remotely controlled by visible light irradiation, with rapid acceleration and deceleration attributed to the photothermal effect of the MNP layer in the wall. Because *E. coli* can survive in NH_3BH_3 solutions, H_2-evolving micromotors show promise as versatile tools for life science applications. ConA-coated tube micromotors successfully captured live *E. coli* without harming the cells. Furthermore, Ure-powered micromotors densely wrapped with Dox-loaded liposomes efficiently attached to cancer cells and released Dox upon NIR irradiation, exhibiting high anticancer activity. Beyond oncology, this strategy may reduce dependence on conventional antibiotics and help mitigate the emergence of drug-resistant strains. Potential *in vivo* applications include operation in urea-rich environments such as the urinary bladder. It is feasible to synthesize a diverse set of photocurable polymer-based tubular micromotors and immobilize proteins, enzymes, antibodies, and metal oxides on their surfaces. These self-propelled polymer tubes thus represent a promising platform for active and targeted applications in the life sciences.

For future practical applications, acrylic-resin tube micromotors present several advantages. The first major hurdle is large-scale production. The PC template-assisted method is well suited to mass production, as microporous PC membranes are already manufactured using track-etching technology, where heavy ion beams irradiate PC thin films and the created minute holes are enlarged by chemical etching. Large-area microporous membranes can be directly employed, and polymer tube walls can be fabricated simply by UV irradiation, making the process both time- and cost-efficient.

A second key hurdle is biosafety. The in-template photopolymerization strategy is applicable to constructing hollow cylinders from biocompatible polymers. The tubes, composed primarily of polyesters and polyelectrolytes, are advantageous for life science applications. In addition, surface functionalization

via wet LbL assembly enables the immobilization of multiple enzymes or catalysts in hierarchical arrangements along the cylindrical wall, facilitating functional relays of sequential reactions. For instance, sandwiching glucoamylase and GOD as intermediate layers in Cat tubes could yield starch-fueled micromotors. Functionally engineered and custom-designed polymer tube micromotors are expected to establish a new paradigm in smart biomaterials science and serve as innovative ultrasmall devices for various biological and biomedical applications.

Conflicts of interest

There are no conflicts to declare.

Data availability

No primary research results, software or code have been included and no new data were generated or analyzed as part of this Feature Article.

Acknowledgements

This work was supported by JSPS KAKENHI Grant Number JK24K01302 and JK25K22923, and JST SPRING Grant Number JMPJST2170.

References

1 H. Wang and M. Pumera, *Chem. Rev.*, 2015, **115**, 8704–8735.
2 M. Safdar, S. U. Khan and J. Jänis, *Adv. Mater.*, 2018, **30**, 1703660.
3 J. Kim, P. Mayorga-Burrezo, S. J. Song, C. C. Mayorga-Martinez, M. Medina-Sánchez, S. Pané and M. Pumera, *Chem. Soc. Rev.*, 2024, **53**, 9190–9253.
4 B. Xu, B. Zhang, L. Wang, G. Huang and Y. Mei, *Adv. Funct. Mater.*, 2018, **28**, 1705872.
5 W. Wang, Z. Wu, X. Lin, T. Si and Q. He, *J. Am. Chem. Soc.*, 2019, **141**, 6601–6608.
6 X. Lu, H. Shen, Y. Wei, H. Ge, J. Wang, H. Peng and W. Liu, *Small*, 2020, **16**, 2003678.
7 X. Lu, Y. Wei, H. Ou, C. Zhao, L. Shi and W. Liu, *Small*, 2021, **17**, 2104516.
8 L. Yang, X. Chen, L. Wang, Z. Hu, C. Xin, M. Hippler, W. Zhu, Y. Hu, J. Li, Y. Wang, L. Zhang, D. Wu and J. Chu, *Adv. Funct. Mater.*, 2019, **29**, 1905745.
9 Z. Wu, T. Si, W. Gao, X. Lin, J. Wang and Q. He, *Small*, 2016, **12**, 577–582.
10 X. Li, R. Wu, H. Chen, T. Li, H. Jiang, X. Xu, X. Tang, M. Wan, C. Mao and D. Shi, *ACS Appl. Mater. Interfaces*, 2021, **13**, 30930–30940.
11 Y. Ying, J. Plutnar and M. Pumera, *Small*, 2021, **17**, 2100294.
12 A. A. Solovev, Y. Mei, E. B. Ureña, G. Huang and O. G. Schmidt, *Small*, 2009, **5**, 1688–1692.
13 A. A. Solovev, S. Sanchez, M. Pumera, Y. F. Mei and O. G. Schmidt, *Adv. Funct. Mater.*, 2010, **20**, 2430–2435.
14 W. Gao, S. Sattayasamitsathit, J. Orozco and J. Wang, *J. Am. Chem. Soc.*, 2011, **133**, 11862–11864.
15 A. A. Solovev, W. Xi, D. H. Gracias, S. M. Harazim, C. Deneke, S. Sanchez and O. G. Schmidt, *ACS Nano*, 2012, **6**, 1751–1756.
16 G. Zhao and M. Pumera, *Langmuir*, 2013, **29**, 7411–7415.
17 G. Zhao, A. Ambrosia and M. Pumera, *Nanoscale*, 2013, **5**, 1319–1324.
18 Y. Li, J. Wu, Y. Xie and H. Ju, *Chem. Commun.*, 2015, **51**, 6325–6328.
19 H. Wang, J. G. S. Moo and M. Pumera, *ACS Nano*, 2016, **10**, 5041–5050.
20 A. Jodra, F. Soto, M. A. Lopez-Ramirez, A. Escarpa and J. Wang, *Chem. Commun.*, 2016, **52**, 11838–11841.
21 P. Wrede, M. Medina-Sánchez, V. M. Fomin and O. G. Schmidt, *Small*, 2021, **17**, 2006449.
22 S. Kobayakawa, Y. Nakai, M. Akiyama and T. Komatsu, *Chem. – Eur. J.*, 2017, **23**, 5044–5050.
23 Y. Nakai, N. Sugai, H. Kusano, Y. Morita and T. Komatsu, *ACS Appl. Nano Mater.*, 2019, **2**, 4891–4899.
24 H. Wang, G. Zhao and M. Pumera, *J. Am. Chem. Soc.*, 2014, **136**, 2719–2722.
25 W. Z. Teo, H. Wang and M. Pumera, *Chem. Commun.*, 2016, **52**, 4333–4336.
26 M. Safdar, O. M. Wani and J. Jänis, *ACS Appl. Mater. Interfaces*, 2015, **7**, 25580–25585.
27 M. Safdar, T. D. Minh, N. Kinnunen and J. Jänis, *ACS Appl. Mater. Interfaces*, 2016, **8**, 32624–32629.
28 W. Liu, H. Ge, Z. Gu, X. Lu, J. Li and J. Wang, *Small*, 2018, **14**, 1802771.
29 S. Sanchez, A. A. Solovev, Y. Mei and O. G. Schmidt, *J. Am. Chem. Soc.*, 2010, **132**, 13144–13145.
30 J. Orozco, V. García-Gradilla, M. D'Agostino, W. Gao, A. Cortes and J. Wang, *ACS Nano*, 2013, **7**, 818–824.
31 Z. Wu, X. Lin, X. Zou, J. Sun and Q. He, *ACS Appl. Mater. Interfaces*, 2015, **7**, 250–255.
32 S. Fu, X. Zhang, Y. Xie, J. Wu and H. Ju, *Nanoscale*, 2017, **9**, 9026–9033.
33 Z. Zheng, X. Zheng, D. Kong, K. Ding, Z. Zhang, R. Zhong, J. He and S. Zhou, *Small*, 2023, **19**, 2207252.
34 N. Sugai, Y. Nakai, Y. Morita and T. Komatsu, *ACS Appl. Nano Mater.*, 2018, **1**, 3080–3085.
35 M. Umebara, N. Sugai, K. Murayama, T. Sugawara, Y. Akashi, Y. Morita, R. Kato and T. Komatsu, *Mater. Adv.*, 2021, **2**, 6428–6438.
36 D. Kagan, S. Campuzano, S. Balasubramanian, F. Kuralay, G.-U. Flechsig and J. Wang, *Nano Lett.*, 2011, **11**, 2083–2087.
37 S. Balasubramanian, D. Kagan, C.-M. J. Hu, S. Campuzano, M. J. Lobo-Castañon, N. Lim, D. Y. Kang, M. Zimmerman, L. Zhang and J. Wang, *Angew. Chem., Int. Ed.*, 2011, **50**, 4161–4164.
38 S. Campuzano, J. Orozco, D. Kagan, M. Guix, W. Gao, S. Sattayasamitsathit, J. C. Claussen, A. Merkoçi and J. Wang, *Nano Lett.*, 2012, **12**, 396–401.
39 M. Luo, Y. Jiang, J. Su, Z. Deng, F. Mou, L. Xu and J. Guan, *Chem. – Asian J.*, 2019, **14**, 2503–2511.
40 C. C. Mayorga-Martinez and M. Pumera, *Adv. Funct. Mater.*, 2020, **30**, 1906449.
41 X. Bing, X. Zhang, J. Li, D. H. L. Ng, W. Yang and J. Yang, *J. Mater. Chem. A*, 2020, **8**, 2809–2819.
42 G. C. Cogal, P. K. Das, G. Y. Karaca, V. R. Bhethanabotla and A. U. Oksuz, *ACS Appl. Bio Mater.*, 2021, **4**, 7932–7941.
43 Jyoti, J. Muñoz and M. Pumera, *ACS Appl. Mater. Interfaces*, 2023, **15**, 58548–58555.
44 J. Orozco, A. Cortés, G. Cheng, S. Sattayasamitsathit, W. Gao, X. Feng, Y. Shen and J. Wang, *J. Am. Chem. Soc.*, 2013, **135**, 5336–5339.
45 S. M. Beladi-Mousavi, J. Klein, B. Khezri, L. Walder and M. Pumera, *ACS Nano*, 2020, **14**, 3434–3441.
46 Z. Wu, Y. Wu, W. He, X. Lin, J. Sun and Q. He, *Angew. Chem. Int. Ed.*, 2013, **52**, 7000–7003.
47 V. V. Singh, K. Kaufmann, B. Esteban-Fernández de Ávila, E. Karshalev and J. Wang, *Adv. Funct. Mater.*, 2016, **26**, 6270–6278.
48 S. M. Beladi-Mousavi, B. Kheizri, L. Krejčová, Z. Heger, Z. Sofer, A. C. Fisher and M. Pumera, *ACS Appl. Mater. Interfaces*, 2019, **11**, 13359–13369.
49 Q. Wang, Y. Wang, B. Guo, S. Shao, Y. Yu, X. Zhu, M. Wan, B. Zhao, C. Bo and C. Mao, *J. Mater. Chem. B*, 2019, **7**, 2688–2695.
50 M. Kamankesh, D. K. Aghmiouni and S. Khoee, *ACS Appl. Nano Mater.*, 2024, **7**, 10056–10067.
51 L. Soler, V. Magdanz, V. M. Fomin, S. Sanchez and O. G. Schmidt, *ACS Nano*, 2013, **7**, 9611–9620.
52 S. Wang, Z. Jiang, S. Ouyang, Z. Dai and T. Wang, *ACS Appl. Mater. Interfaces*, 2017, **9**, 23974–23982.
53 K. Villa, J. Parmar, D. Vilela and S. Sánchez, *ACS Appl. Mater. Interfaces*, 2018, **10**, 20478–20486.
54 C. Liang, C. Zhan, F. Zeng, D. Xu, Y. Wang, W. Zhao, J. Zhang, J. Guo, H. Feng and X. Ma, *ACS Appl. Mater. Interfaces*, 2018, **10**, 35099–35107.

55 W. Liu, H. Ge, X. Chen, X. Lu, Z. Gu, J. Li and J. Wang, *ACS Appl. Mater. Interfaces*, 2019, **11**, 16164–16173.
56 W. Liu, H. Ge, X. Ding, X. Lu, Y. Zhang and Z. Gu, *Nanoscale*, 2020, **12**, 19655–19664.
57 L. Chen, H. Yuan, S. Chen, C. Zheng, X. Wu, Z. Li, C. Liang, P. Dai, Q. Wang, X. Ma and X. Yan, *ACS Appl. Mater. Interfaces*, 2021, **13**, 31226–31235.
58 J. Wang, J. Si, Y. Hao, J. Li, P. Zhang, C. Zuo, B. Jin, Y. Wang, W. Zhang, W. Li, R. Guo and S. Miao, *Langmuir*, 2022, **38**, 1231–1242.
59 H. Cui, K. Wang, E. Ma and H. Wang, *Nanomaterials*, 2023, **13**, 2710.
60 X. Yang, C. Liu, S. Gao, X. Zhang, Z. Lan, M. Zuo and J. Li, *Environ. Sci.: Nano*, 2024, **11**, 1142–1156.
61 N. Xing, Y. Lyu, W. Zhao, Z. Lan, M. Zuo and J. Li, *Environ. Sci.: Nano*, 2024, **11**, 3162–3177.
62 M. García, J. Orozco, M. Guix, W. Gao, S. Sattayasamitsathit, A. Escarpa, A. Merkoçic and J. Wang, *Nanoscale*, 2013, **5**, 1325–1331.
63 Y. Su, Y. Ge, L. Liu, L. Zhang, M. Liu, Y. Sun, H. Zhang and B. Dong, *ACS Appl. Mater. Interfaces*, 2016, **8**, 4250–4257.
64 Á. Molinero-Fernández, A. Jodra, M. Moreno-Guzmán, M. Á. López and A. Escarpa, *Chem. – Eur. J.*, 2018, **24**, 7172–7176.
65 Á. Molinero-Fernández, M. Moreno-Guzmán, L. Arruza, M. Á. López and A. Escarpa, *ACS Sens.*, 2020, **5**, 1336–1344.
66 Á. Molinero-Fernández, M. Á. López and A. Escarpa, *Anal. Chem.*, 2020, **92**, 5048–5054.
67 V. de la Asunción-Nadal, M. Pacheco, B. Jurado-Sánchez and A. Escarpa, *Anal. Chem.*, 2020, **92**, 9188–9193.
68 J. Bujalance-Fernández, B. Jurado-Sánchez and A. Escarpa, *Anal. Chem.*, 2024, **96**, 10791–10799.
69 Á. Gallo-Orive, M. Moreno-Guzmán, M. Sanchez-Paniagua, A. Montero-Calle, R. Barderas and A. Escarpa, *Anal. Chem.*, 2024, **96**, 5509–5518.
70 A. Escarpa and B. Jurado-Sánchez, *Anal. Chem.*, 2025, **97**, 12913–12924.
71 Z. Wu, X. Lin, T. Si and Q. He, *Small*, 2016, **12**, 3080–3093.
72 B. Esteban-Fernández de Ávila, P. Angsantikul, J. Li, W. Gao, L. Zhang and J. Wang, *Adv. Funct. Mater.*, 2018, **28**, 1705640.
73 C. Gao, Y. Wang, Z. Ye, Z. Lin, X. Ma and Q. He, *Adv. Mater.*, 2021, **33**, 2000512.
74 W. Gao, S. Sattayasamitsathit, A. Uygun, A. Pei, A. Ponedala and J. Wang, *Nanoscale*, 2012, **4**, 2447–2453.
75 R. Maria-Hormigos, B. Jurado-Sanchez, L. Vazquez and A. Escarpa, *Chem. Mater.*, 2016, **28**, 8962–8970.
76 B. Zhang, G. Huang, L. Wang, T. Wang, L. Liu, Z. Di, X. Liu and Y. Mei, *Chem. – Asian J.*, 2019, **14**, 2479–2484.
77 B. Newland, C. Taplan, D. Pette, J. Friedrichs, M. Steinhart, W. Wang, B. Voit, F. P. Seib and C. Werner, *Nanoscale*, 2018, **10**, 8413–8421.
78 R. María-Hormigos, Á. Molinero-Fernández, M. Á. López, B. Jurado-Sánchez and A. Escarpa, *Anal. Chem.*, 2022, **94**, 5575–5582.
79 X. Ma, A. C. Hortelao, A. Miguel-López and S. Sánchez, *J. Am. Chem. Soc.*, 2016, **138**, 13782–13785.
80 L. Wang, P. Guo, D. Jin, Y. Peng, X. Sun, Y. Chen, X. Liu, W. Chen, W. Wang, X. Yan and X. Ma, *ACS Nano*, 2023, **17**, 5095–5107.
81 N. Sugai, Y. Morita and T. Komatsu, *Chem. – Asian J.*, 2019, **14**, 2953–2957.
82 H. Wang, G. Zhao and M. Pumera, *J. Phys. Chem. C*, 2014, **118**, 5268–5274.
83 J. Simmchen, V. Magdanz, S. Sanchez, S. Chokmaviroj, D. Ruiz-Molina, A. Baeza and O. G. Schmidt, *RSC Adv.*, 2014, **4**, 20334–20340.
84 D. Pantarotto, W. R. Browne and B. L. Feringa, *Chem. Commun.*, 2008, 1533–1535.
85 W. Gao, A. Uygun and J. Wang, *J. Am. Chem. Soc.*, 2012, **134**, 897–900.
86 W. Gao, R. Dong, S. Thamphiwatana, J. Li, W. Gao, L. Zhang and J. Wang, *ACS Nano*, 2015, **9**, 117–123.
87 B. Esteban-Fernández de Ávila, M. A. Lopez-Ramirez, R. Mundaca-Uribe, X. Wei, D. E. Ramírez-Herrera, E. Karshalev, B. Nguyen, R. H. Fang, L. Zhang and J. Wang, *Adv. Mater.*, 2020, **32**, 2000091.
88 J. Li, S. Thamphiwatana, W. Liu, B. Esteban-Fernández de Ávila, P. Angsantikul, E. Sandraz, J. Wang, T. Xu, F. Soto, V. Ramez, X. Wang, W. Gao, L. Zhang and J. Wang, *ACS Nano*, 2016, **10**, 9536–9542.
89 Z. Wan, C. H. Y. Chung, C. M. L. Lau, J. T. Chung, Y. Chau, Z. Fan, S. Zhang and S. Yao, *Nano Lett.*, 2025, **25**, 5989–5996.
90 S. K. Srivastava, M. Guix and O. G. Schmidt, *Nano Lett.*, 2016, **16**, 817–821.
91 S. Zachariah, K. Kumar, S. W. H. Lee, W. Y. Choon, S. Naeem and C. Leong, *Clinical Pharmacy Education, Practice and Research*, ed. D. Thomas, Elsevier, 2019, ch. 7, pp. 91–108.
92 L. Liu, H. Mo, S. Wei and D. Raftery, *Analyst*, 2012, **137**, 595–600.
93 M. Hashimoto, Y. Akashi, Y. Sakai, T. Sugawara, R. Kato, B. Schade, K. Ludwig and T. Komatsu, *ACS Appl. Polym. Mater.*, 2024, **6**, 5822–5832.
94 Y. Akashi, N. Sugai, R. Kato and T. Komatsu, *Mater. Adv.*, 2022, **3**, 6988–6992.
95 V. Moulès, O. Terrier, M. Yver, B. Riteau, C. Moriscot, O. Ferraris, T. Julien, E. Giudice, J.-P. Rolland, A. Erny, M. Bouscambert-Duchamp, E. Frobert, M. Rosa-Calatrava, Y. P. Lin, A. Hay, D. Thomas, G. Schoehn and B. Lina, *Virology*, 2011, **414**, 51–62.
96 S. Batori and T. Komatsu, *ACS Appl. Nano Mater.*, 2024, **7**, 6804–6809.
97 Q. Feng, B. Tang, Q. Wei, D. Hou, S. Bi and A. Wei, *Int. J. Mol. Sci.*, 2012, **13**, 12734–12746.
98 Z. Wu, X. Lin, Y. Wu, T. Si, J. Sun and Q. He, *ACS Nano*, 2014, **8**, 6097–6105.
99 J. G. S. Moo, S. Presolski and M. Pumera, *ACS Nano*, 2016, **10**, 3543–3552.
100 R. M. Hormigos, B. J. Sánchez and A. Escarpa, *Angew. Chem. Int. Ed.*, 2019, **58**, 3128–3132.
101 Y. Zhao, M. E. Sadat, A. Dunn, H. Xu, C.-H. Chen, W. Nakasuga, R. C. Ewing and D. Shi, *Sol. Energy Mater. Sol. Cells*, 2017, **161**, 247–254.
102 A. Staubitz, A. P. M. Robertson and I. Manners, *Chem. Rev.*, 2010, **110**, 4079–4124.
103 B. Gong, H. Wu, L. Sheng, W. Zhang and X. Wu, *ACS Appl. Mater. Interfaces*, 2022, **14**, 13231–13239.
104 M. Muzzio, H. Lin, K. Wei, X. Guo, C. Yu, T. Yom, Z. Xi, Z. Yin and S. Sun, *ACS Sustainable Chem. Eng.*, 2020, **8**, 2814–2821.
105 M. Hashimoto, Y. Sakai, T. Yamada, R. Kato and T. Komatsu, *ACS Appl. Bio Mater.*, 2024, **7**, 7740–7747.
106 S. Batori and T. Komatsu, *ACS Appl. Nano Mater.*, 2025, **8**, 11763–11768.